Abstract

In this work, rotors with artificial iced shapes are studied to develop insight in the potential of acoustics-based ice detection. Using the Helicopter Multi-Block CFD solver, approximate iced shapes are added to the blades and the results are analyzed using the FW-H method. Several candidate monitoring positions are assessed for acoustic sensors to be placed on the helicopter fuselage. The influence of ice on the aero-acoustic characteristics of a rotor is calculated, and parameters such as the ice amount and the icing position on the blade are quantified. It is concluded that an array of microphones is best for detecting potential icing position on the blades, and it should be located on top of the helicopter rear fuselage and along the tail-boom.

Keywords

CFD, aero-acoustic characteristics, ice accretion, rotor, helicopter

Introduction

Helicopter blade icing can be a serious threat to flight safety[1] since it modifies the aerodynamic shape of the rotor blades and degrades its aerodynamic performance[2,3]. At present, there are two main approaches to deal with icing[4]. First, pilots are given weather information and try to avoid potential icing conditions. Second, aircraft are thoroughly deiced before take-off and then operate ice protection systems (IPS) for in-flight ice removal. At present, only 5% of the US rotorcrafts are equipped with an IPS[5]. For aircraft without IPS, the general rule is to avoid flying in icing conditions. Compared to fixed-wing aircraft, helicopter icing is not well understood due to complexities in the 3-D rotor flow environment with inherent unsteady flow, rotational movement of rotor and strong centrifugal forces on the blades[6,7]. The best way to deal with icing is early detection since pilots can make use of the IPS or change their flight plan to avoid flying within icing conditions. For the above reasons, ice detection has become critically important for helicopter safety and efficiency.

Many sensors using different technologies have so far been developed to detect ice formation on aircraft surfaces[8,9]. An ice detection system consists of a resonant piezoelectric sensing-element and a microprocessor controller, and it can sense ice and water films up to 0.5 mm thick[10].

Another approach investigated, was based on scatter of light in the iced volume[11]. All these sensors are difficult to deploy due to the limited space inside blades[12]. In addition, due to the complex motion of rotors, such as rotor flapping, regular ice detection methods like infrared detectors[13] are also difficult to implement on rotors.

According to previous studies[14,15], the change of the flow behavior and blade shape by ice accretion is likely to affect the helicopter main rotor noise. Cheng's studies[16] also show that rotor noise can be used to detect the formation of ice at the early stage of ice accretion. Anyway, there are few other studies of helicopter noise during ice accretion found in the open literature. A noise monitor, such as a microphone array, which does not have to be mounted on the rotor, is easier to deploy on helicopter fuselage, and there is no need for rotor blade modifications. In addition, several works have already been published on the aero-acoustic characteristics on rotors[17,18]. These developments make the ice detection by rotor aero-acoustic characteristics possible.

Based on the Helicopter Multi-Block (HMB) CFD code[19], the objective of the present work is to analyze the variation of aero-acoustic characteristics of iced rotors, and identify microphone positions that are suitable for detecting ice accretion. First, comparisons are presented against available test data in the open literature, then the hover acoustics of rotors with different ice amounts and with ice at different positions along the blade are investigated. The effect of icing in forward flight is then analyzed. The sensitivity of the acoustic characteristics to ice accretion is finally considered, and microphone positions are suggested for possible installation on a helicopter as part of an ice detection system.

Helicopter multi-block CFD solver

The HMB solver was employed in this work. HMB solves the unsteady Reynolds-averaged Navier-Stokes equations on block-structured grids using a cell centered finite-volume method for spatial discretization. Implicit time integration is employed, and the resulting linear system of equations is solved using a pre-conditioned Generalized Conjugate Gradient method. For unsteady simulations, an implicit dual time stepping method is used. The method has been validated for a wide range of aerospace applications and has demonstrated good accuracy and efficiency for very demanding flows[20].

Aerodynamic and acoustic method

Based on the CFD air loads obtained by the HMB solver, the Ffowcs-Williams Hawkings (FWH) method is used for calculating the aero-acoustic characteristic of clean and iced rotors[21]. The FWH theory is derived by combining the equations of mass and momentum conservation for compressible fluids, to obtain an inhomogeneous wave equation. This equation governs the generation and propagation of sound waves in a volume outside any closed surface. The Farassat 1A equation to be solved for the FWH is as follows

$$p(\mathbf{x},t) = p_T(\mathbf{x},t) + p_L(\mathbf{x},t), \tag{1}$$

where $p_T'(x,t)$ and $p_L'(x,t)$ are the thickness and load noise respectively. For an arbitrary rotor-observer distance the thickness and load noise components can be written as

$$4\pi p_T(\mathbf{x},t) = \int_{f=0}\left[\frac{\rho_0 v_n\{r\dot{\mathrm{M}}_r + c_0(\mathrm{M}_r - \mathrm{M}^2)\}}{r^2(1-\mathrm{M}_r)^3}\right]_{ret} ds + \int_{f=0}\left[\frac{\rho_0(\dot{v}_n + v_{\dot{n}})}{r(1-\mathrm{M}_r)^2}\right]_{ret} ds, \tag{2}$$

and

$$4\pi p_L(\mathbf{x},t) = \int_{f=0}\left[\frac{\dot{l}_i\hat{r}_i}{r(1-\mathrm{M}_r)^2}\right]_{ret} ds + \frac{1}{c_0}\int_{f=0}\left[\frac{l_r - l_i M_i}{r^2(1-\mathrm{M}_r)^2}\right]_{ret} ds + \int_{f=0}\left[\frac{l_r(r\dot{\mathrm{M}}_i\hat{r}_i + c_0\mathrm{M}_r - c_0\mathrm{M}^2)}{r^2(1-\mathrm{M}_r)^2}\right]_{ret} ds. \tag{3}$$

Here t is observer time; c_0 is the speed of sound; ρ_0 is the air density; v_n is the normal velocity of the surface; M is the local rotational Mach number; $\mathrm{M}_r = \mathrm{M}_i\hat{r}_i$ is the Mach number of source in radiation direction; $r = |\mathbf{x}-\mathbf{y}|$ is the distance between observer and source, $\mathbf{x}$ is the observer position vector, and $\mathbf{y}$ is the source position vector. The above expressions also include $l_r = l_i r_i$, with l_i force/unit area on the medium, and the radiation direction $\hat{\mathbf{r}}$ at the time of emission. A dot over variables is used as a symbol of differentiation with respect to the time of the emission source. The subscript *ret* stands for the

retarded time with the integration evaluated over the emission surface $f = 0$. For the FW-H equation numerical (CFD) simulation results are used for the acoustic pressure (p) at source. This formulation is used in the current work to estimate the Effective Sound Pressure (ESP) at different positions.

Calculated results and analyses

Aerodynamic characteristics of the NACA23012 airfoil with and without ice

The experimental data for an iced NACA23012 airfoil, obtained at the NASA Langley Low Turbulence Pressurized Tunnel (LTPT) is selected to validate the accuracy of the numerical method. The LTPT measurements[22] were at a Mach number of 0.208 and at a Reynolds number of approximately 2×10^5.

Figure 1 shows a detailed view of the ice shape and the modified NACA23012 section. The ice amount is very small, and the radius of the ice is only 0.0139*c*.

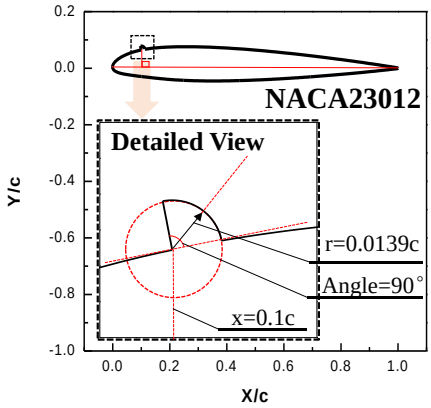

Figure 1. Detailed view of the ice shape and the modified NACA23012 section.

Figure 2 shows the aerodynamic characteristics of the NACA23012 with and without ice. The comparisons of the lift and drag coefficients (C_L and C_D) with experimental data show fair agreement (except near stall where the steady-state flow assumption). When ice forms on the airfoil, the lift force decreases, and the drag force increases.

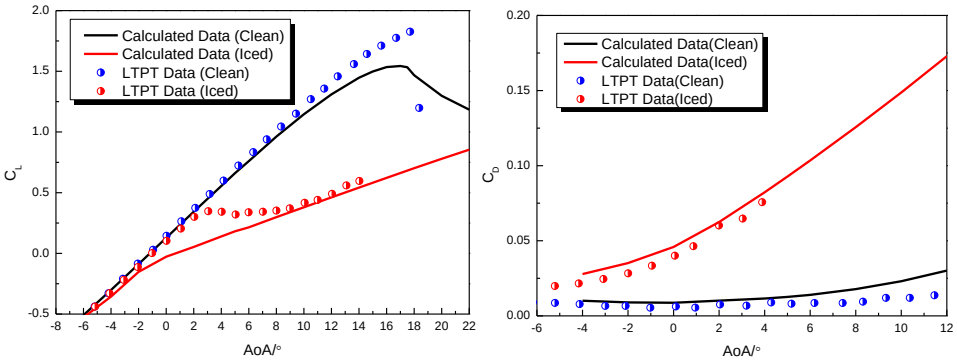

(a) C_L (b) C_D

Figure 2. Lift (a) and drag (b) coefficients vs the angle of attack for the NACA 23012 airfoil with and without ice.

Figure 3 shows pressure coefficient (C_p) distributions on the airfoil surface with and without ice, at 0° of the angle of attack. As shown, the calculated results are in good agreement with LTPT data, indicating that the present CFD solver is reliable for simulating the aerodynamic characteristics of the iced airfoils.

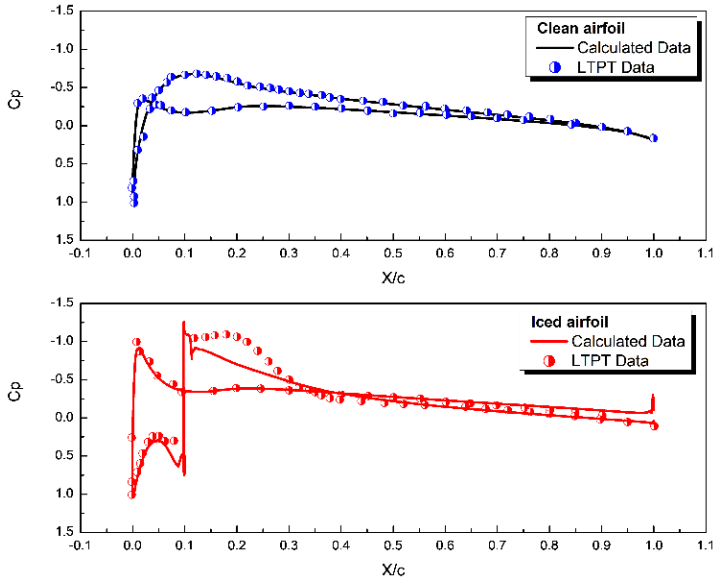

Figure 3. Pressure coefficient distributions of NACA 23012 airfoil with and without ice.

Acoustic characteristics of rotors in hover with and without ice

The Caradonna-Tung (C-T) rotor is selected to analyze the variation of acoustic characteristics of iced rotors in hover. The C-T rotor has two rectangular blades with a conventional NACA 0012 airfoil. For

the iced rotor, the icing positions were from 0.6R to 0.9R along the blade. Figure 4 shows the icing position on the C-T rotor and sectional ice shapes.

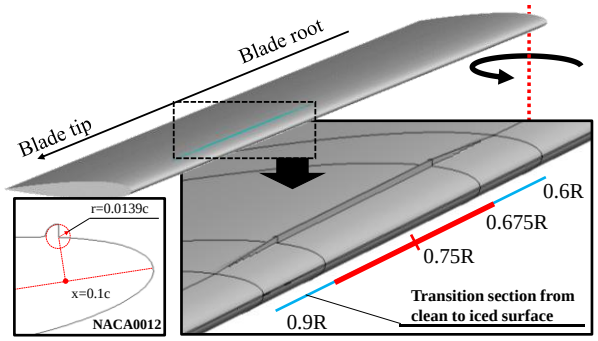

Figure 4. Icing position on the C-T rotor and sectional ice shape.

Clean and iced cases for this rotor at M_{tip}=0.794 and at Re=3.48×10^6 were calculated. Table 1 shows the variation of the aerodynamic performance of the rotor in hover with and without ice at a collective pitch of 8°.

Table 1. Variation of aerodynamic performances (C_T the rotor rust coefficient, C_Q is the rotor torque coefficient, and FM is the Figure of Merit) of rotor in hover with and without ice.

Aerodynamic characteristics	C_T	C_Q	FM
Clean Rotor	1.10×10^{-2}	1.17×10^{-3}	0.492
Iced Rotor	0.61×10^{-2}	1.54×10^{-3}	0.156
Variation	-44.1%	+31.5%	-68.2%

In addition, Figure 5 presents the comparison of the sectional pressure distribution of the clean C-T rotor with experiment data. As can be seen, the numerical results are in a good agreement with experiments [23].

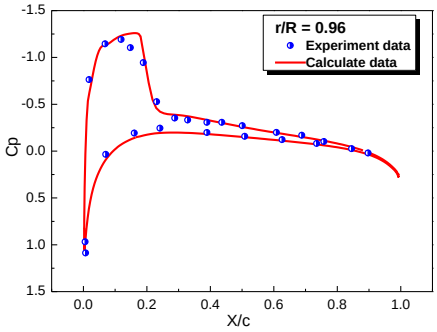

Figure 5. Comparison of the sectional pressure distribution of clean C-T rotor with experiment data.

Although the iced area is small compared with the blade sectional area, the deterioration of the aerodynamic characteristics is obvious, as seen in Table 1. There is a decrease of about 70 percent in the

Figure of Merit (FM). This is not only qualifying the strong influence of ice on the rotor aerodynamic performance, but also the importance of ice detection on rotor blades. Given that most of the aerodynamic thrust is produced outboards on the blade, the selected location for the ice is expected to has a strong influence on its performance.

Some monitoring points placed relative to the blade for ice detection are shown in Figure 6. Considering the installation of acoustic monitors on the fuselage, all monitors are below the rotating plate, and their location is defined by the polar coordinates (r, z).

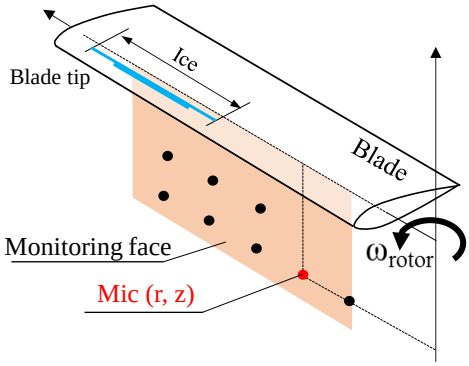

Figure 6. Positions of acoustics monitors relative to the blade.

Figure 7 shows the Effective Sound Pressure (ESP) at different monitor positions, between clean and iced rotors. There are significant differences in the obtained acoustics. This is because the lift force of the iced rotor drops. On the $z = -0.25R$ plane, the ESP of the iced rotor first increases and then decreases compared to the clean rotor near the blade root. On the $z = -0.5R$ plane, the ESP of the iced rotor decreases compared with the clean rotor. In general, for small ice pieces the emitted blade noise level is proportional to the blade load (also see Figure 10); further decrease of lift leads to lower ESP values.

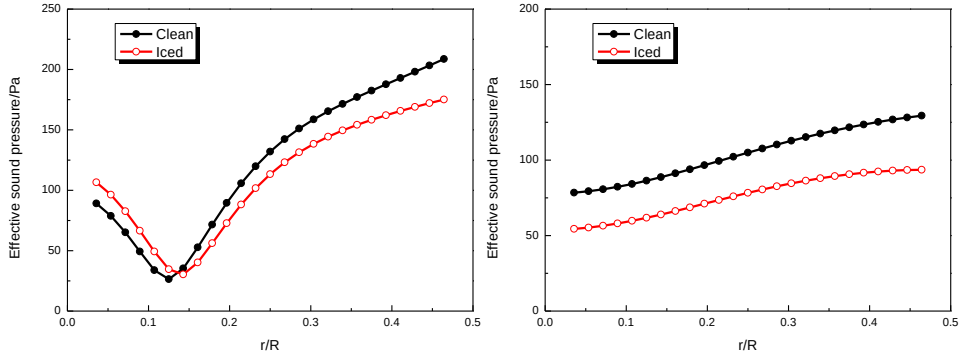

Figure 7. ESP at different monitor positions for clean and iced rotors: (a) z=-0.25R; (b) z=-0.5R.

The differences of the ESP at different *z* planes are shown in Figure 8. When the monitor is far away from the rotor plane, the ESP of all monitors at the different radial positions decrease. When monitors are close to the rotor plane, the ESP changes significantly in the radial direction. It increases in places, and decreases in others. However, the variation of sound pressure is evident in this case, indicating that ice can be detected based on the variation of the blade acoustic characteristics.

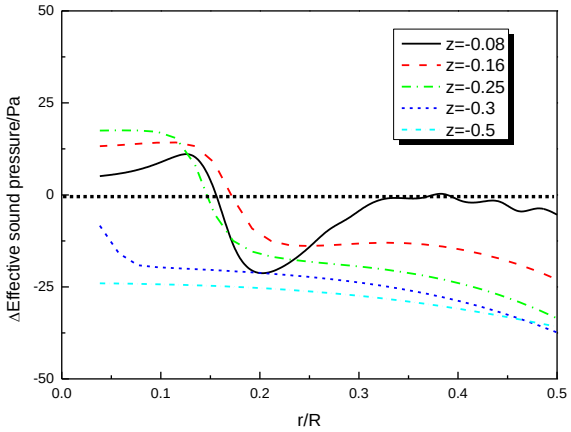

Figure 8. Difference of the ESP between clean and iced rotors at different *z* planes.

To further analyze the acoustics variations, Figure 9 shows the differences of the ESP at different points of the observation area. The data is obtained using the from FWH method using the computed effective sound pressure levels on a grid that is then used to produce the colored contours. It is assumed that the acoustic monitor can detect changes in sound pressure bigger than 10 Pa. For this iced rotor, as long as the acoustic monitor is in the yellow or blue region, ice can be detected.

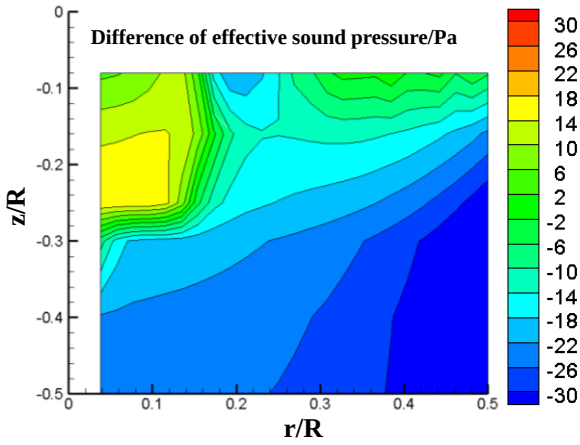

Figure 9. Difference of the effective sound pressure between clean and iced rotors.

In addition, the sound pressure time histories of a typical monitoring position ($r = 0.25R$, $z = -0.25R$) are given in Figure 10. The difference in the ESP for this position is 15 Pa. As can be seen, the main difference of the ESP comes from loading noise, while the thickness noise is almost unchanged. Considering the large variation of the aerodynamic characteristics in this case, the acoustic characteristics of some iced rotors with shorter ice lengths were also calculated.

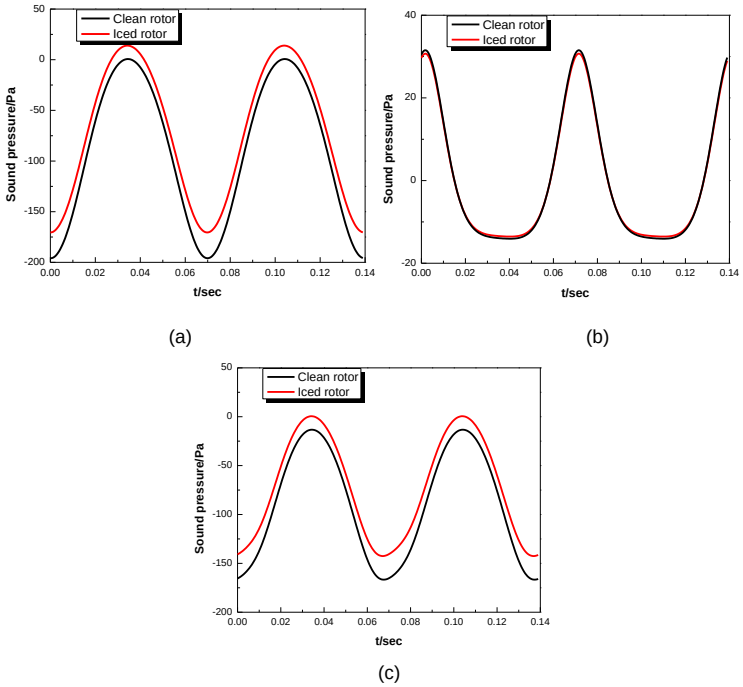

Figure 10. Sound pressure time histories at a typical monitoring position: Loading noise (a); Thickness noise (b); Total noise (c).

Acoustic characteristics of iced rotor with different ice amount

Three rotors with different ice lengths are added to analyze the variation of acoustic characteristics, as seen in Figure 11. Rotor A is the previously used iced rotor, and its ice length is 0.3*R*. The ice length of rotor D is the shortest, only 0.033*R*.

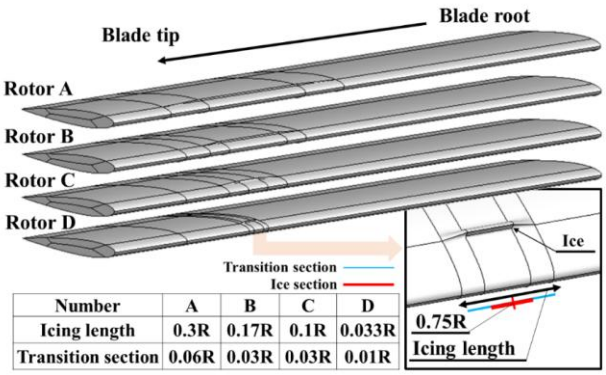

Number	A	B	C	D
Icing length	0.3R	0.17R	0.1R	0.033R
Transition section	0.06R	0.03R	0.03R	0.01R

Figure 11. Ice lengths used for analysis.

Table 2 shows the aerodynamic characteristics of the rotors at the same condition, M_{tip}=0.794, Re=3.48×10^6 and for the collective pitch of 8°. With the decrease in the ice length, the variation of aerodynamic characteristics of the rotor decreases. For rotor D, the variation of FM is only 7.69%.

Table 2. Aerodynamic performance of different iced rotors in hover.

Aerodynamic characteristics	C_T	C_Q	FM	Variation of FM
Clean	1.10×10^{-2}	1.17×10^{-3}	0.492	
Rotor A	0.61×10^{-2}	1.54×10^{-3}	0.156	-68.2%
Rotor B	0.91×10^{-2}	1.36×10^{-3}	0.318	-35.4%
Rotor C	1.04×10^{-2}	1.29×10^{-3}	0.409	-16.8%
Rotor D	1.06×10^{-2}	1.21×10^{-3}	0.454	-7.69%

Figure 12 shows the sound pressure time histories of two typical monitoring points with the radial coordinate $r = 0.25R$: $z = -0.25R$ and $z = -0.3R$. As seen, the sound pressure of rotor A decreases compared with the clean rotor, and the sound pressures of rotors C and D slightly increase. This is more obvious on the $z = -0.3R$ plane, because iced rotors with less ice maintain good aerodynamic characteristics.

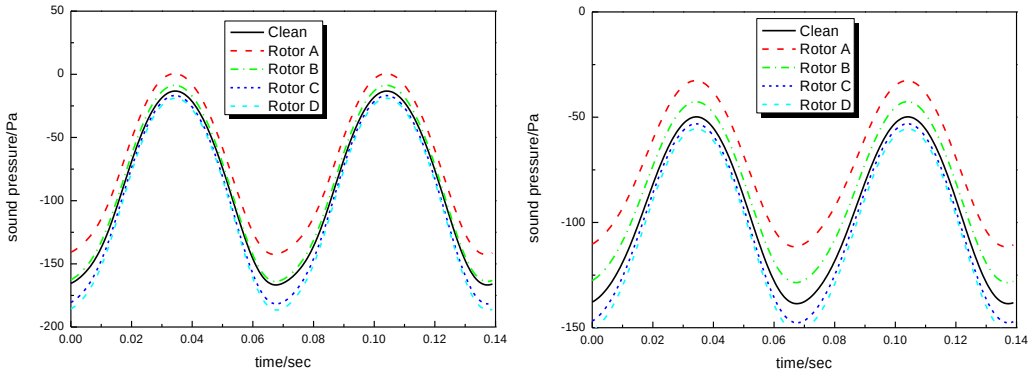

Figure 12. Sound pressure time histories of two monitoring positions at *r*=0.25*R*: *z*=-0.25*R* (a); *z*=-0.3*R* (b).

For rotor B at the considered point ($r = 0.25R$: $z = -0.25R$) the ESP level is identical to the clean rotor (Figure 12a). The same can be seen in Figures 13 and 14 that show ESP on the $z = -0.25R$ plane, and the differences in ESP between various rotors and the clean one. When the ice length is small, the ESP decreases near the blade root and increases near the middle of the blade along the radius (R). As shown in Figure 10, the variation of the thickness noise is very small due to the formed ice. Therefore, the variation of the loading noise is the main reason behind the observed changes in the total sound pressure. A piece of ice of small limited length can only change the aerodynamic loading close to its location, and so the differences in noise seen for rotor B are small near $(r = 0.25R, z = -0.25R)$, and larger near $(z = 0.25, z = -0.3R)$,as seen in Figure 12.

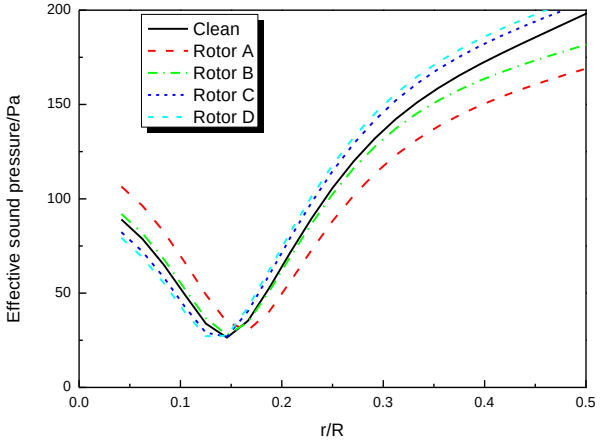

Figure 13. ESP with different monitoring positions on the *z*=-0.25*R* plane.

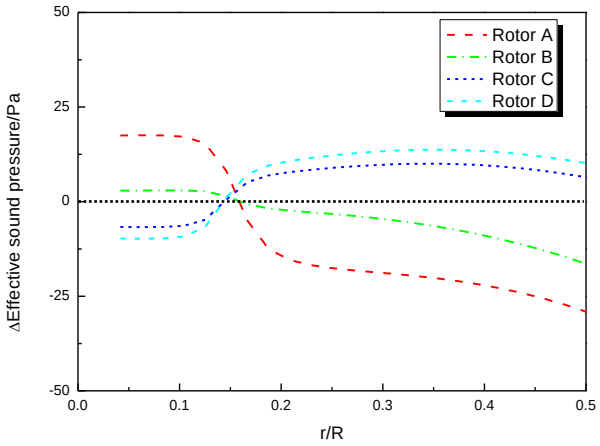

Figure 14. Differences of ESP on the *z*=-0.25*R* plane.

During the early stage of ice accretion, the ice length is normally short. Thus, ice detection for rotors with short ice lengths is more important.

Figure 15 shows the comparison of the ESP between the clean rotor and the iced rotor D, at different monitor positions. When the monitor is far away from the rotation plane, the ESP of rotor D is very close to the clean rotor. When the monitor is far away from the rotation plane ($z = -0.5R$, $z = -0.3R$), the ESP of rotor D is very close to the clean rotor and blade the ESP of the iced rotor is higher than for the clean rotor. When the monitor position is close to the rotation plane, the ESP of the iced rotor first is less than for the clean rotor (at the root part of the blade); for the rest part of blade the ESP of the iced rotor is higher in comparison to the clean rotor. To show this, the differences of the ESP at different z planes are given in Figure 16.

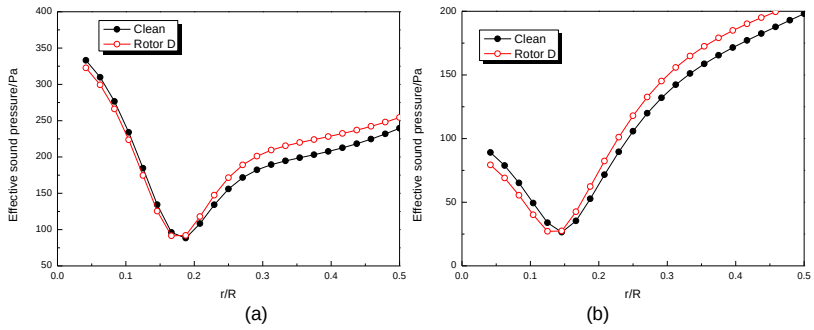

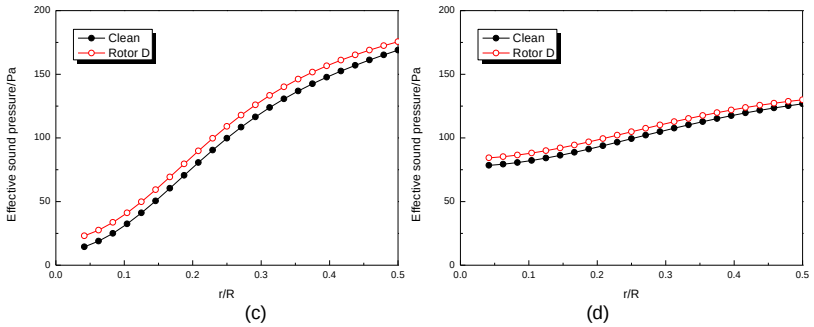

Figure 15. ESP at different monitor positions between clean and D rotors: z=-0.16R (a), z=-0.25R (b), z=-0.3R (c), z=-0.5R (d).

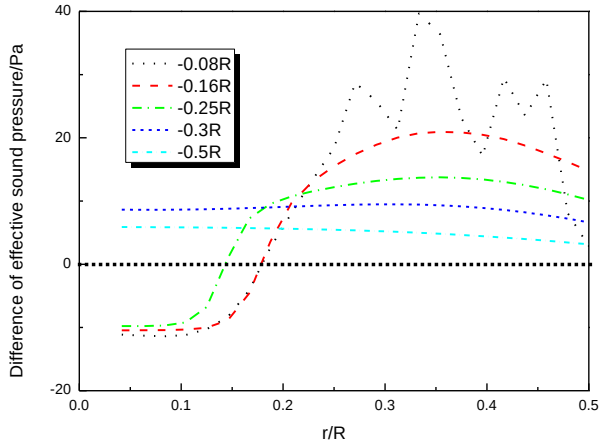

Figure 16. Difference of the ESP between clean rotor and rotor D, at different z planes.

As seen (Figure 16), even if the ice length is very short, the variation of the acoustic characteristics of the rotor is still apparent. This indicates that the small variation of the blade shape, at the early stage of ice accretion, can be detected by the variation of the blade acoustic characteristics.

More detailed information about the differences in ESP at different monitoring positions for rotor D is presented in Figure 17. In the yellow and green regions, the difference of ESP is too low, and the acoustic monitor cannot detect the ice. In the red regions, the ESP increases. As a result, these regions are appropriate for monitor installation. Similarly, the blue region is also a good monitoring area, although the ESP decreases there.

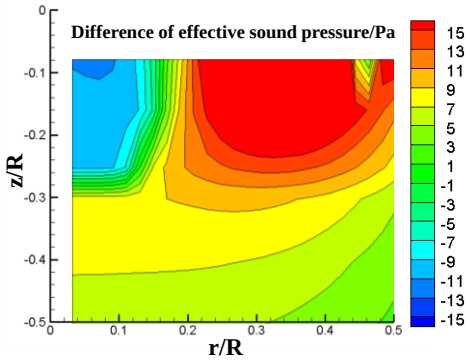

Figure 17. ESP difference at different monitoring positions between the clean rotor, and rotor D.

Acoustic characteristics of iced rotors with different icing positions

Two iced rotors with different icing position are added to analyze the influence of the icing position on the acoustic characteristics, as shown in Figure 18. The ice length and ice shape of these two iced rotors are the same as rotor D, the only difference is the icing position. The icing position of rotor E is from 0.53*R* to 0.56*R*, and that of rotor F is from 0.33*R* to 0.36*R*.

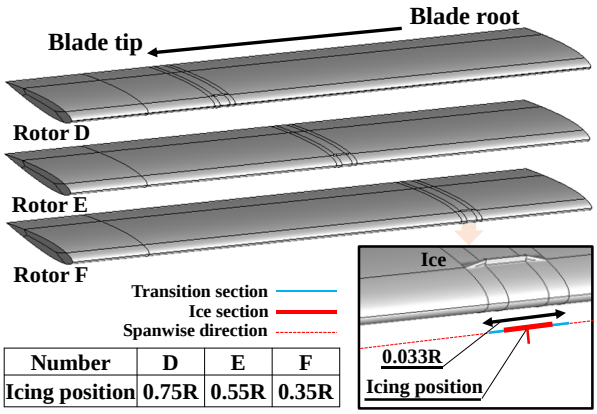

Number	D	E	F
Icing position	0.75R	0.55R	0.35R

Figure 18. Different icing positions used for analysis.

Table 3 shows the aerodynamic characteristics of the iced rotors at the same condition, M_{tip}=0.794, Re=3.48×10^6 and collective pitch of 8°. With ice moving to the blade root, the variation of the FM decreases. However, the ice accretion has little effect on the aerodynamic characteristics of these three rotors.

Отформатировано: Английский (США)

Table 3. Aerodynamic performance of different iced rotors in hover.

Aerodynamic characteristics	C_T	C_Q	FM	Variation of FM
Clean	1.10×10^{-2}	1.17×10^{-3}	0.492	
Rotor D	1.06×10^{-2}	1.21×10^{-3}	0.454	-7.69%
Rotor E	1.07×10^{-2}	1.20×10^{-3}	0.461	-6.31%
Rotor F	1.07×10^{-2}	1.18×10^{-3}	0.468	-4.87%

Figure 19 shows the ESP of different iced rotors below the rotor plane.

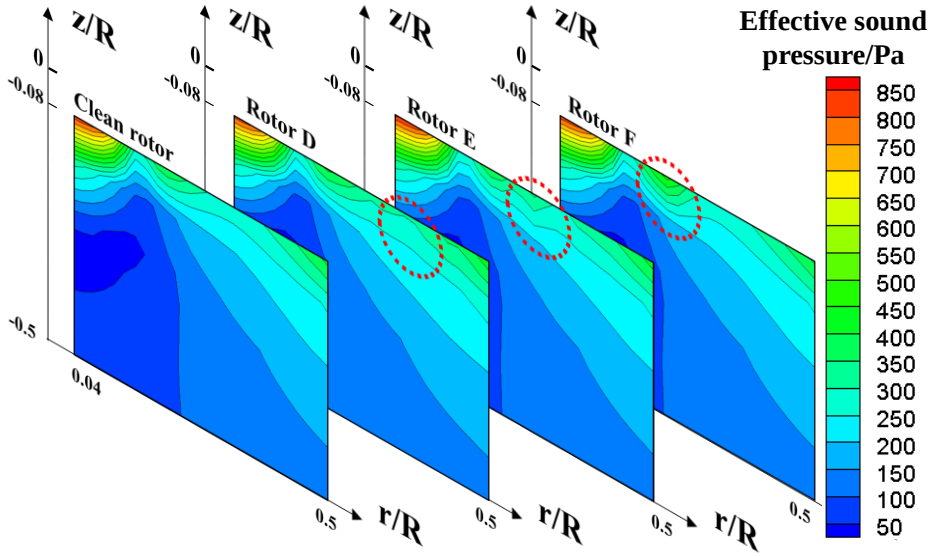

Figure 19. The ESP of different iced rotors below the rotor plane in hover.

For all rotors considered, the main changes in ESP are concentrated near the blade icing position. Since the ice amounts on rotors E and F are very small, the changes of the ESP are not appreciable. However, the influence of the icing position on the ESP of the rotor is clear, as shown in the figure.

The distribution of the differences in ESP between the clean and the iced rotors E and F are shown in Figure 20 on a plane below the blade. For rotor E, the obvious variation area (differences greater than 5 or less than 5 Pa) is from $r = 0.1R$ to $r = 0.42R$ along the radial direction and near the $z = -0.15R$ plane. For rotor F, the obvious variation area is from $r = 0.1R$ to $r = 0.3R$ along the radial direction and near the $z = -0.2R$ plane. Combining with Figure 17, ice can change the ESP in a limited area, and this area is from the blade root to the icing position along the radial direction.

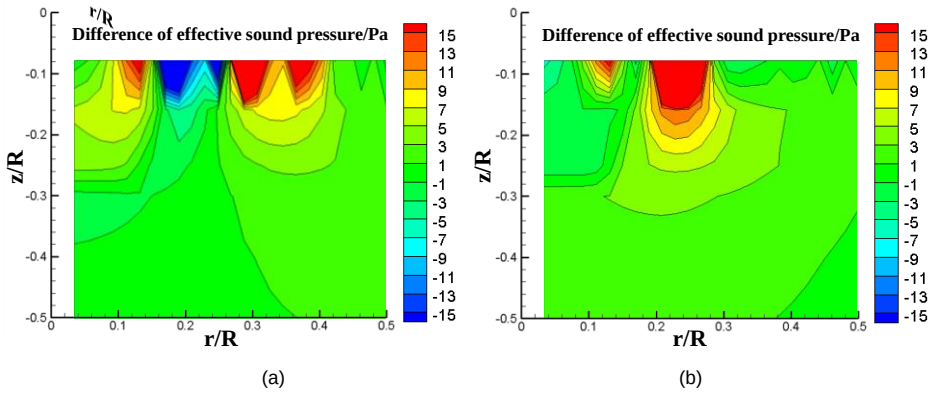

Figure 20. The difference of ESP between iced rotors and clean rotor: rotor E (a), rotor F (b).

For comparison purposes, the absolute values of the difference of the ESP between these iced rotors and the clean rotor on the $z = -0.16R$ plane are given in Figure 21. The actual pressure values are given so that the magnitude of the differences to be detected by potential sensors on the helicopter fuselage is evident. As can be seen, when the icing position is closer to the blade tip, such as for rotor D, the region of the ESP variation is larger. When the icing position is closer to the blade root, such as for rotor F, the region of the ESP variation is small.

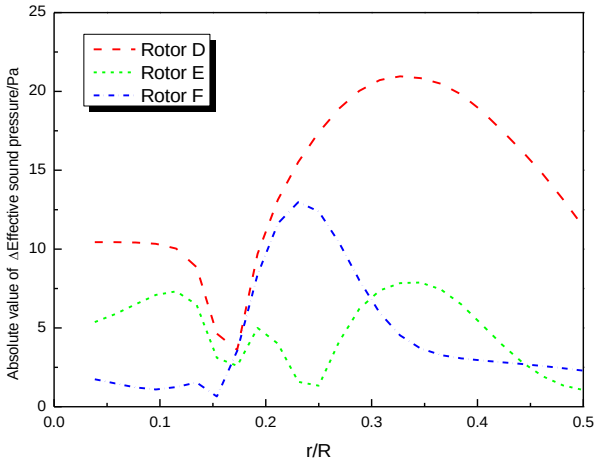

Figure 21. The difference in the ESP between these iced rotors and the clean rotor on the *z*=-0.16*R* plane.

In addition, the comparisons of the total sound pressure time histories at four monitoring positions on the $z = -0.16R$ plane are given in Figure 22. At $r = 0.1R$, the sound pressure time histories of rotor F and the clean rotor are nearly the same, while there are obvious changes for rotors D and E. Then, the changes for rotor F are evident at $r = 0.2R$, and decrease at $r = 0.3R$. There are no appreciable differences between rotor F and the clean rotor.

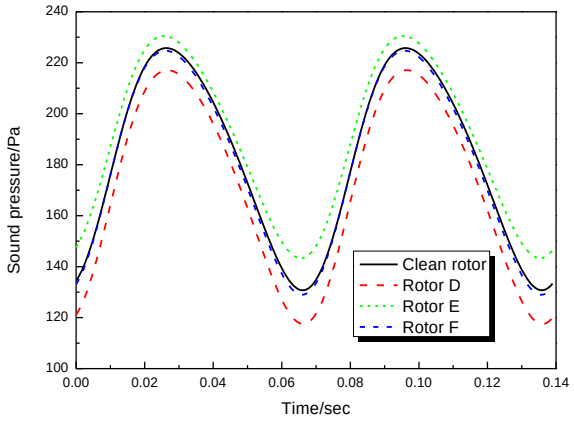

(a)

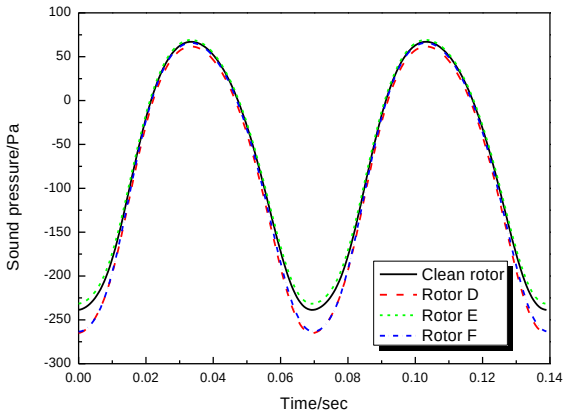

(b)

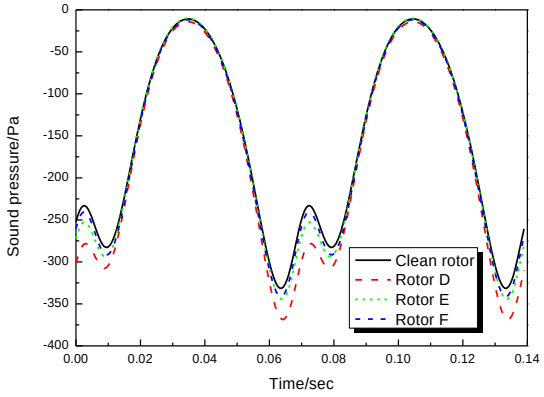

(c)

Figure 22. The comparison of total sound pressure time histories at three monitoring positions on the z=-0.16R plane: r=0.1R (a), r=0.2R (b), r=0.3R (c).

As a result, through the variations of the sound pressure at different monitoring points, the icing position can be detected, especially if several monitors are used. Since the fuselage shapes differ between helicopters, it is assumed that the fuselage is a simple hemisphere with a radius of 0.3*R* and a half cylinder with a radius of 0.125*R*.

In Figure 22, the icing positions of rotors D, E and F are different, but their ice lengths are the same. As seen, when the monitoring position is 0.1*R*, the variation of rotors D and E are larger, since the ice is closer to 0.1*R* than for rotor F. The sound pressure of rotor D decreases, and that of the rotor E increases. This is because the changes of their aerodynamic loadings are different. The sound pressure of Rotor F is closer to the clean rotor, because the ice, which is near 0.7*R*, has a small influence on the air loads. In Figure 22(c), there are small variations of the sound pressure near the middle of the plot. This is due to the differences in the peak values of the thickness and loading components of the noise.

Based on the above, a monitor array located on the surface of the fictitious fuselage is used to detect potential icing on the blades. The monitors are distributed on the surface of the imaginary fuselage, and the coordinates are also given in Figure 23(a). Figure 24(b) shows the calculated result at these monitors for different iced rotors. As seen, there is significant variation of the ESP obtained from each monitor (A-F) and for each blade (D-F).

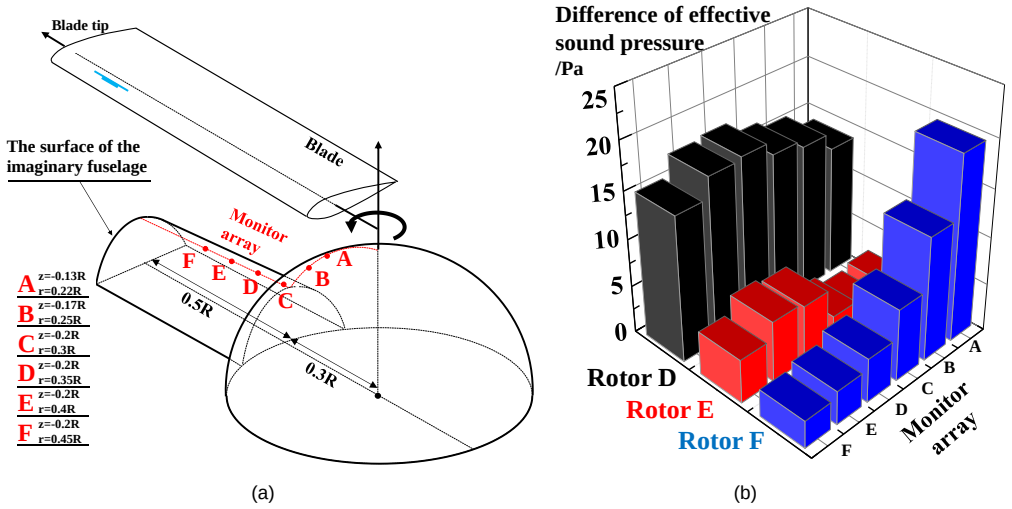

Figure 23. The ice detection using by the monitor array: relative position (a), monitor array (b).

For this hovering case, an assumption is made that the sensitivity of the monitors is greater than 5 Pa. Figure 24 shows the monitoring result transformed from Figure 23(b) and the relationship between the monitor array (with/without activation) and the icing position. As seen, for rotor D (with icing position is 0.7*R*), the monitors are all activated. For rotor E (icing position is 0.5*R*), the monitors D and E are activated. For rotor F (icing position is 0.3*R*), monitors A, B and C are activated. Actually, if the ice length is longer than 0.03*R*, all monitors are active. Since a long ice piece near the blade root may have the same effect on the sound pressure as a short ice piece near the blade tip, it is difficult to obtain the icing position and ice length at the same time from the monitor array.

However, regardless of the influence of the ice length, a potential icing position can be still obtained from the monitor array. For this case, if monitors (D, E and F) are not activated, ice may not be detected on the blade from 0.3*R* to the blade tip. If monitors (A, B and C) are not activated, ice may not be detected on the blade from the blade root to 0.3*R* section. If monitor F is not activated, ice may not be detected on the blade from 0.5*R* to the blade tip. If all monitors are activated, ice can be detected anywhere on the blade. If the number of monitors in a monitor array is larger, a more accurate potential icing position will be obtained.

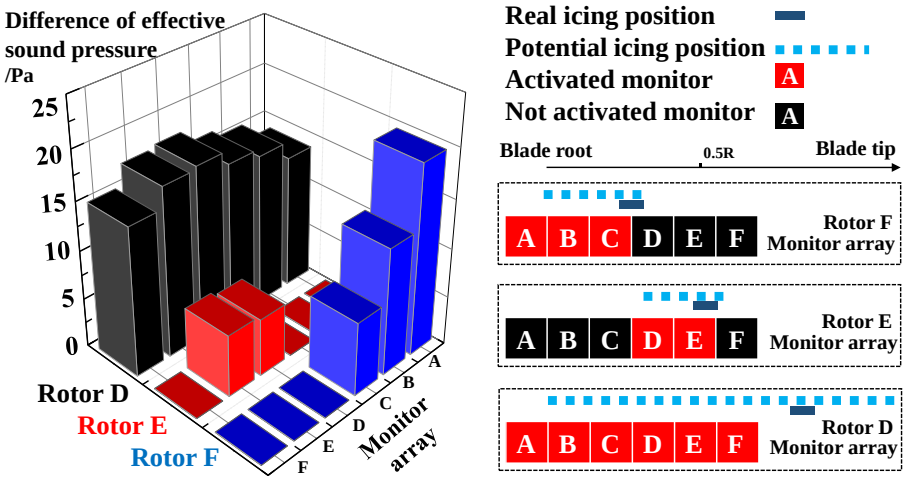

Figure 24. The ice detection result obtained from the monitor array.

Acoustic characteristics of rotors in forward flight with a short ice shape

UH-60A rotors with and without ice are also computed in forward flight. Figure 25 shows the comparison of the sectional lift coefficients of the clean rotor with experiment data at M_{tip}=0.642 and μ=0.368. As can be seen, the numerical results are in good agreement with experiments[24].

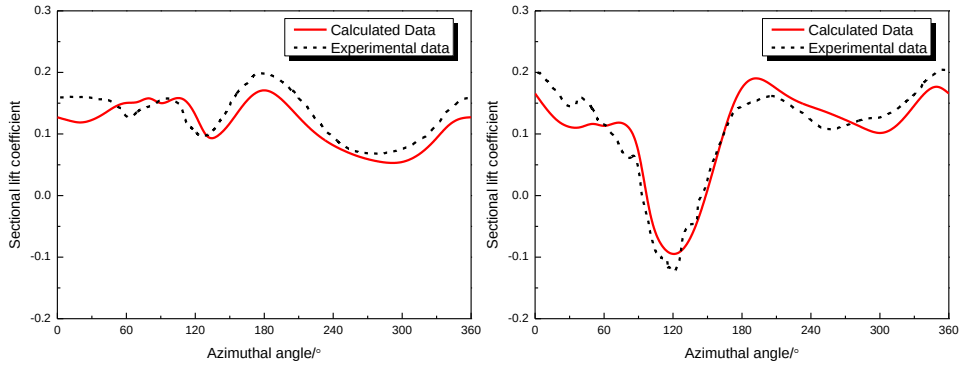

(a) (b)

Figure 25. Sectional lift coefficient of the UH-60A rotor in forward flight: *r*=0.675*R* (a), *r*=0.865*R* (b).

Two iced rotors with different icing position are also computed to analyze the influence of ice on the acoustic characteristics in forward flight. The ice length and ice shape of these two iced rotors are the same, as shown in Figure 26. The icing position of rotor G is from 0.594*R* to 0.606*R*, and that of rotor H is from 0.694*R* to 0.706*R*.

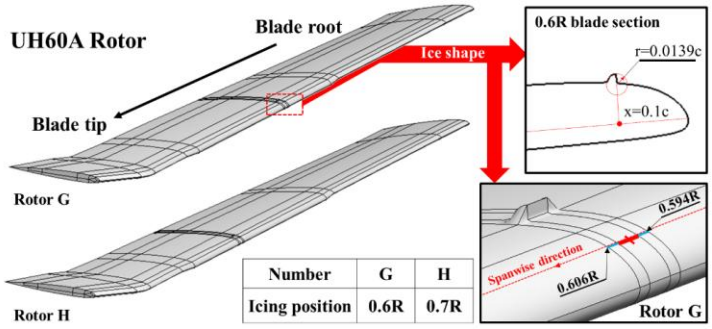

Figure 26. Different icing positions used for analysis in forward flight case.

Figure 27 shows the sectional lift coefficient of the UH-60A rotor with and without ice in forward flight. At $r = 0.5R$, there is no difference between the clean and iced rotors. At $r = 0.6R$, there is an obvious difference between rotor G and the clean rotor, while there are no appreciable differences between rotor H and the clean rotor. At $r = 0.7R$, there is an obvious difference in the range from 60° to 270° of azimuth angles between rotor H and the clean rotor. Figure 28 presents the sectional torque coefficient of the UH-60A rotor with and without ice in forward flight. It can be seen that the small ice can only change the loading in a limited region along the spanwise direction, and the loading differences are too small for the overall rotor. So, in this case, ice is difficult to be detected by the variation of the aerodynamic characteristics.

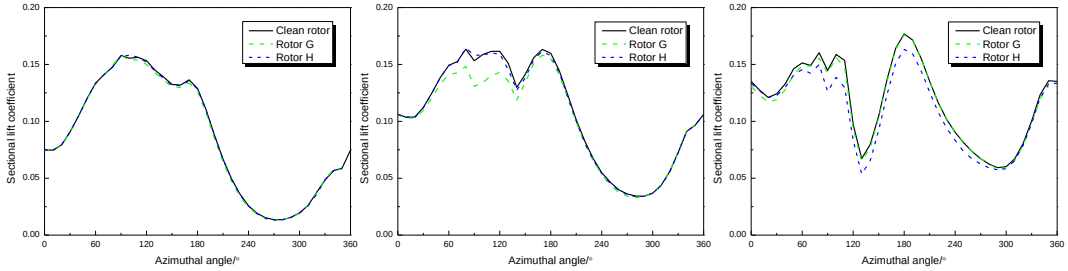

(a) (b) (c)

Figure 27. Sectional lift coefficient of the UH-60A rotor with and without ice in forward flight: *r*=0.5*R* (a), *r*=0.6*R* (b), *r*=0.7*R* (c).

The difference of the ESP between the clean UH-60A rotor and rotor G is shown in Figure 29. The monitoring area is in a range from 0.15*R* to 0.48*R* along the radial direction and from -0.1*R* to -0.4*R*

along the vertical direction. As seen in the figure, the difference of ESP is strong enough to be used for ice detection, and the acoustic characteristic variations are different around the azimuth, unlike hover.

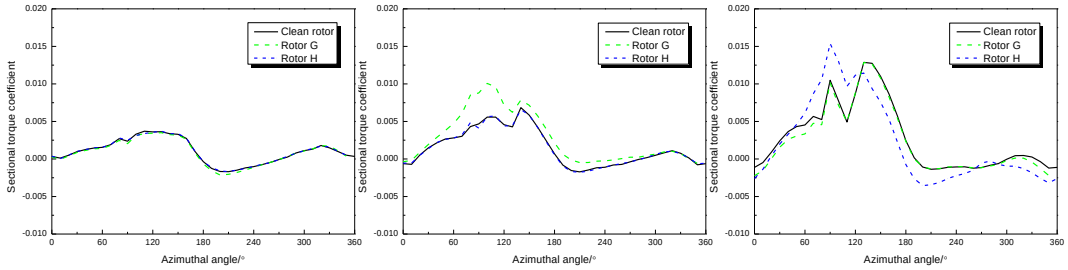

(a) (b) (c)

Figure 28. Sectional torque coefficient of the UH-60A rotor with and without ice in forward flight mode: *r*=0.5*R* (a), *r*=0.6*R* (b), *r*=0.7*R* (c).

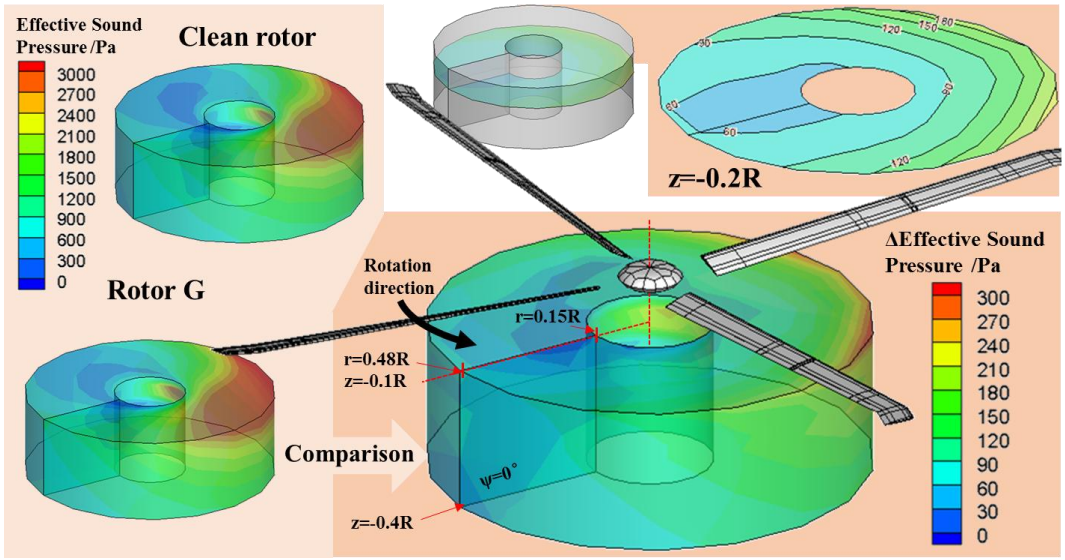

Figure 29. Difference of the ESP of the clean UH60A rotor and rotor G.

To clarify, Figure 30 shows the difference of the ESP at different *z* planes between the clean rotor and rotor G. The difference of the ESP is larger in a range from 90° to 270° of azimuthal angle. When the monitor is far away from the rotor plane (from $z = -0.1R$ to $z = -0.3R$), the difference of the ESP decreases. Additionally, Figure 31 shows the difference of the ESP at different *y* planes between a clean rotor and rotor G. Compared with the difference at the 180° of azimuth angle, the variation of the ESP is smaller and less violent at 0° azimuth.

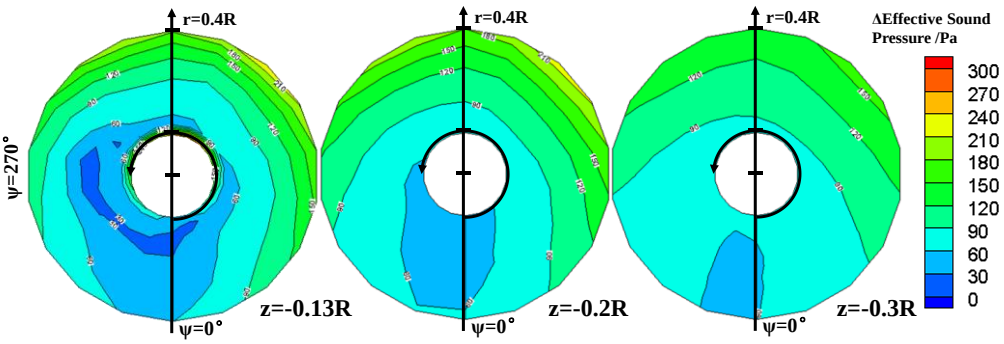

Figure 30. Difference of the ESP at different z planes between clean rotor and rotor G.

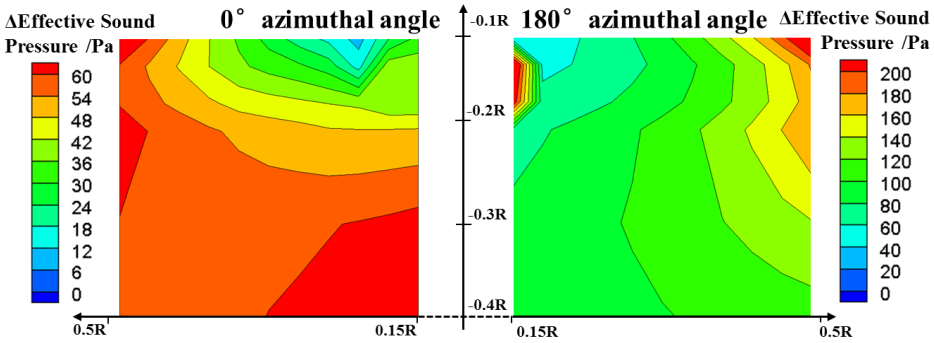

Figure 31. Difference of the ESP at different *y* planes between clean rotor and rotor G.

Based on the above, Figure 32 shows the differences in ESP at 0° of azimuth angle between the iced and clean rotors. As seen, the difference of the ESP of rotor H is greater than the rotor G, since the icing positions are different.

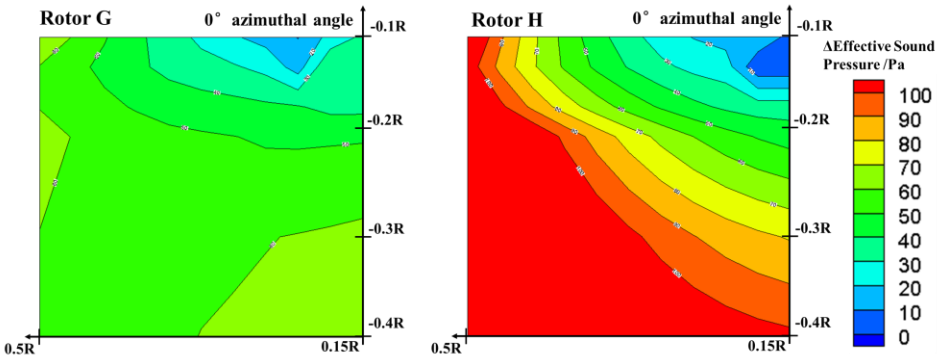

Figure 32. Difference of ESP at different y planes between clean rotor and rotor G.

Finally, the monitor array (shown in Figure 23) is used to detect potential icing position on the UH-60A rotor in forward flight. Figure 33 shows the ice detection results obtained from the monitor array.

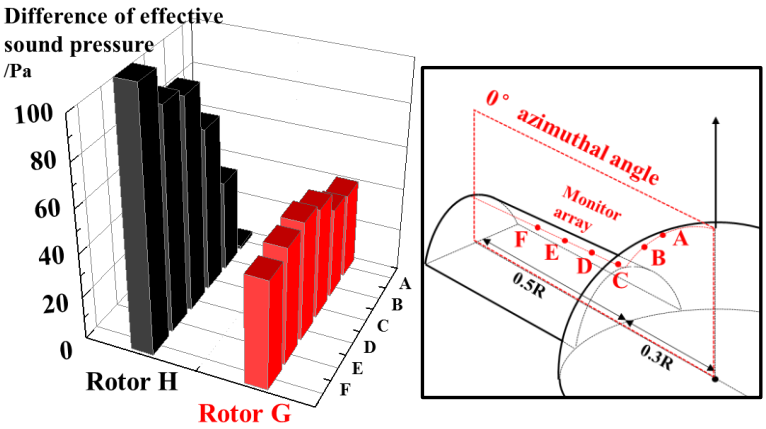

Figure 33. Difference of the ESP obtained from the monitor array.

Considering that the loading is much greater than that in the hover case, the difference of the ESP is also greater. For this forward flight case, an assumption is given that the monitors have a sensitivity of 50 Pa. Based this assumption, Figure 34 shows the potential icing position detected from the monitor array. For this case, monitors (A, B and F) are not activated, and this means that ice may not be detected from the blade root to 0.3*R* and from 0.7*R* to the blade tip. If monitors (A, B) are not activated, ice may not be detected from the blade root to 0.3*R*. Obviously, the potential icing positions obtained from the array are consistent with the real icing position of rotors G and H.

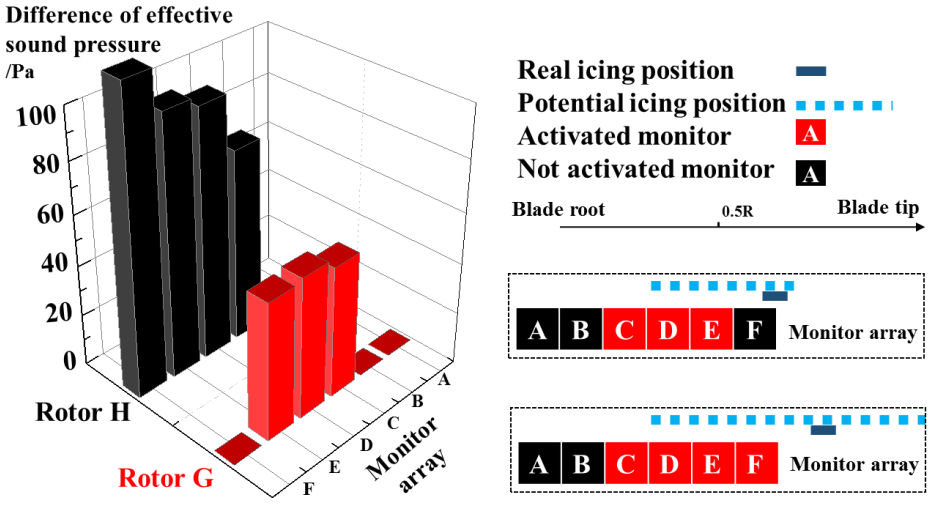

Figure 34. Ice detection result obtained from the monitor array for UH-60A rotor in forward flight.

Conclusion

The aero-acoustic characteristics of rotors are greatly influenced by ice accretion. Overall, the effect of ice on the acoustics increases with the decrease of the vertical distance of the microphone, and slightly increases with the increase of the radial distance. The variation of the thickness noise will be small if the volume of the formed ice on the blade is small. In addition, this work shows that ice on rotors can be detected at certain microphone positions near the rotor plane. If the ice length is short, the sound pressure will only change in a limited region along the blade radius. The current simulations also show that if ice is formed near the blade root, the signal captured by monitors located closer to the blade root changes, while monitors near the blade tip are ineffective. Through variations of the sound pressure at different monitoring points, the icing position on the rotor can be detected, especially if several monitors are used.

Aiming towards a practical implementation, a given monitor array distributed on the surface of the fuselage, a potential icing position on the blade can be obtained. The array of microphones should be located on top of the helicopter rear fuselage and along the tail-boom.

References

1. Hartman P, Narducci R, Peterson A, Dadone L, Mingione G, Zanazzi G and Brandi V. Prediction of ice accumulation and airfoil performance degradation: A Boeing - CIRA research collaboration. *AHS* 62*th Annu Forum*, Phoenix, Arizona, USA 9 - 11 May 2006, pp. 123-146.

2. Cebeci T and Kafyeke F. Aircraft icing. *Annu Rev Fluid Mech* 2003; 35: 11–21.

3. Hemming R, Britton R, Flemming R and Bond T. Results of a sub-scale model rotor icing test. In: *AIAA Pap* 91-0660, 1991.

4. Caliskan F and Hajiyev C. In-flight detection and identification and accommodation of aircraft icing. In: *AIP Conf Proc* 1493, 200, 2012, pp. 200–206.

5. Heinrich A, Ross R, Zumwait G, Provorse J, Padmanabhan V, Thompson J and Riley J. *Aircraft Icing Handbook*. Atlantic City International Airport, NJ: FAA technical Center, 1991.

6. Zhao G, Zhao Q and Chen X. New 3-D ice accretion method of hovering rotor including effects of centrifugal force. *Aerosp Sci Technol* 2016; 48: 122–130.

7. Wang Z and Zhu C. Study of the effect of centrifugal force on rotor blade icing process. *Int J Aerosp Eng* 2017; Article ID 8695170, 9 pages.

8. Dershowitz AL and Hansman RJ Jr. Passive infrared ice detection for helicopter applications. In: *Annual Forum Proc - Am. Helicopter Soc* 1990.

9. Melody JW, Başar T, Perkins WR and Voulgaris PG. Parameter identification for inflight detection and characterization of aircraft icing. *Control Eng Pract* 2000; 8: 985–1001.

10. Roy S, Izad A, DeAnna R and Mehregany M. Smart ice detection systems based on resonant piezoelectric transducers. *Sensors Actuators, A Phys* 1998; 69: 243–250.

11. Ikiades A, Howard G, Armstrong D, Konstantaki M and Crossley S. Measurement of optical diffusion properties of ice for direct detection ice accretion sensors. *Sensors Actuators, A Phys* 2007; 140: 24–31.

12. Jakoby B and Vellekoop M. Viscosity sensing using a Love-wave device. *Sensors Actuators, A Phys* 1998; 68: 275–281.

13. Yin X, Zhang Y, Wang D, Liu Z, Liu Y, Pei X, Yu B and Zhou F. Integration of self-lubrication and near-infrared photothermogenesis for excellent anti-icing/deicing performance. *Adv Funct Mater* 2015; 25: 4237–4245.

14. Chen X, Zhao QJ, Ma YY and Wang B. Mechanism analyses on aeroacoustic characteristics of iced rotor for ice detection. *AHS* 73*th Annu Forum*, Fort Worth, Texas, USA, May 9-11, 2017, pp. 95-104.

15. Chen X and Zhao Q. Numerical simulations for ice accretion on rotors using new three-dimensional icing model. *J Aircr* 2017; 54: 1428–1442.

16. Cheng B, Han Y, Brentner KS, Palacios J, Morris PJ, Hanson DR and Kinzel MP. Rotor broadband noise due to surface roughness during ice accretion. 54*th AIAA Aerosp Sci Meet.*, San Diego, California, USA, 4-8 January 2016, paper no. 1270, pp. 1–16.

17. Francescantonio P Di. A new boundary integral formulation for the prediction of sound radiation. *J Sound Vib* 1997; 202: 491–509.

18. Brentner KS and Farassat F. Analytical comparison of the acoustic analogy and Kirchhoff formulation for moving surfaces. *AIAA J* 1998; 36: 1379–1386.

19. Barakos G, Steijl R, Badcock K and Brocklehurst A. Development of CFD capability for full helicopter engineering analysis. 31*st Eur Rotorcr Forum*, Florence, Italy, 13-15 Sep 2005, paper no. 91, pp. 1–15.

20. Steijl R and Barakos GN. CFD analysis of complete helicopter configurations - Lessons learnt from the GOAHEAD project. *Aerosp Sci Technol* 2012; 19: 58–71.

21. Farassat F. Linear acoustic formulas for calculation of rotating blade noise. *AIAA J* 1981; 19: 1122–1130.

22. Bragg MB, Broeren AP and Blumenthal LA. Iced-airfoil aerodynamics. *Prog Aerosp Sci* 2005; 41: 323–362.

23. Caradonna FX, Laub GH and Tung C. An experimental investigation of the parallel blade-vortex interaction. NASA/TM 86005, 1984.

24. Chopra I, Sitaraman J and Baeder JD. Validation of UH-60A rotor blade aerodynamic characteristics using CFD. *AHS 59th Annu Forum*, Phoenix, Arizona, May 6-8, 2003, pp. 1452-1468.